Counterion Dependent Side-Chain Relaxation Stiffens a Chemically Doped Thienothiophene Copolymer

Advanced Functional Materials

ADVANCED FUNCTIONAL MATERIALS
www.afm-journal.de

RESEARCH ARTICLE OPEN ACCESS

Counterion Dependent Side-Chain Relaxation Stiffens a Chemically Doped Thienothiophene Copolymer

Mariavittoria Craighero[1] | Meghna Jha[1] | Elsa Veronica Flores-Vela[1] | Joost Kimpel[1] | Andreas Schaefer[1] | Jiali Guo[2] | Jesika Asatryan[3] | Alberto Peinador Veiga[3] | Shuichi Haraguchi[1] | Per-Anders Carlsson[1] | Jaime Martín[3] | Mariano Campoy-Quiles[2] | Christian Müller[1]

[1]Department of Chemistry and Chemical Engineering, Chalmers University of Technology, Göteborg, Sweden | [2]Materials Science Institute of Barcelona, ICMAB-CSIC, Campus UAB, Bellaterra, Spain | [3]Universidade da Coruña, Campus Industrial de Ferrol, CITENI, Esteiro, Ferrol, Spain

Correspondence: Christian Müller (christian.muller@chalmers.se)

Received: 24 September 2025 | **Revised:** 28 November 2025 | **Accepted:** 30 December 2025

Keywords: conjugated polymer | chemical doping | density | electrical conductivity | elastic modulus

ABSTRACT

The electrical conductivity and elastic modulus of doped conjugated polymers tend to increase in tandem, which complicates the design of soft conductors. This work investigates how different dopant counterions influence the electrical and mechanical properties of a thienothiophene copolymer with triethylene glycol side chains. Sequential doping and proton-coupled electron-transfer were used to prepare samples with a comparable oxidation level neutralized with different counterions. Highly oxidized films featured a comparable electrical conductivity of about 100 S cm^{-1} irrespective of the counterion size. Dynamic mechanical analysis revealed that the choice of counterion strongly impacts the sub-glass transition temperature, which varied from −44°C to −3°C. As a result, the elastic modulus at room temperature ranged from 0.05 GPa to 0.7 GPa for materials with a comparable oxidation level. Evidently, it is possible to decouple the electrical and mechanical properties of doped polymers, which are governed by charge transport along the backbone and side-chain relaxation, respectively. This insight opens up new opportunities for the design of soft conductors and more sustainable bioelectronic and wearable devices whose various soft and rigid components could be created with the same polymer.

1 | Introduction

Conjugated polymers are appealing for a wide range of applications, from stretchable [1–3] and wearable electronics [4, 5] to soft robotics [6, 7] and bioelectronics [7, 8], all of which require specific mechanical properties. For instance, materials for electronic skin or textiles should be relatively soft since they are to deform during manufacture and use [9]. Instead, stiffer materials are needed for structural components and devices such as thermoelectric generators, in the latter case to create the micrometer-to-millimeter thick structures, i.e., thermoelectric legs, that allow to maintain an out-of-plane thermal gradient [10, 11].

The stiffness of a device is inversely related to its flexibility, and it depends on the intrinsic properties of the materials that it is composed of as well as its geometry [12, 13]. Hence, the stiffness can be reduced by selecting a material with an appropriate elastic modulus and by decreasing the thickness of a device. When the device architecture is predetermined by its electrical performance the material selection plays a crucial role in optimizing flexibility. Conducting polymer-based materials with a wide range of mechanical properties can be obtained by a number of different approaches such as chemical design [14, 15], blending with insulating polymers [2, 16, 17], compounding with nanomaterials [18, 19] and chemical doping [20–22].

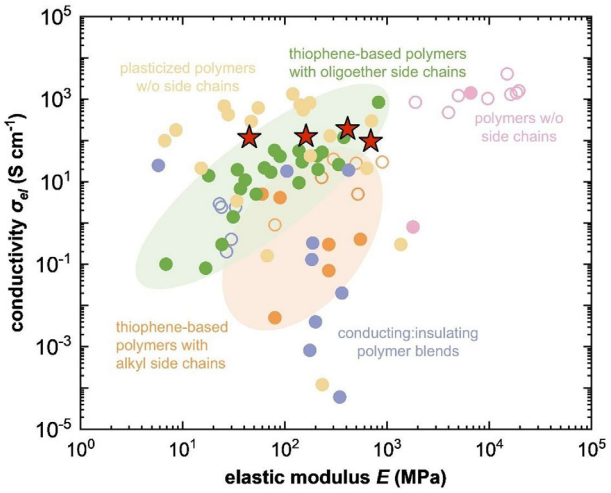

FIGURE 1 | Elastic modulus E vs. electrical conductivity σ_{el} for isotropic (full symbols) and anisotropic (empty symbols) conjugated polymer-based films; data from refs. [2, 5, 17, 18, 20–24, 26, 28–30, 32, 45–50] (circles) and from this work (stars).

The electrical conductivity σ_{el} and elastic modulus E of conjugated polymers tend to correlate (Figure 1). A material with high electrical conductivity is often associated with a high elastic modulus. For example, polymers without side chains synthesized by oxidative polymerization such as poly(3,4-ethylenedioxythiophene):poly(styrenesulfonate) (PEDOT:PSS) and poly(benzodifurandione) (PBFDO) tend to feature values of $\sigma_{el} > 1000$ S cm^{-1} and $E > 1$ GPa [5, 12, 23, 24]. Instead, most doped conjugated polymers with side chains display values of 10 S cm^{-1} $< \sigma_{el} <$ 1000 S cm^{-1} and 0.1 GPa $< E <$ 1 GPa at room temperature, making them suitable for many applications where a softer material is needed [12].

Interestingly, σ_{el} and E also tend to increase in tandem with the oxidation level of conjugated polymers, as for instance observed in case of polythiophenes with oligoether side chains doped with 2,3,5,6-tetrafluoro-tetracyanoquinodimethane (F_4TCNQ), reaching values of $\sigma_{el} = 830$ S cm^{-1} and $E > 0.8$ GPa [20, 22, 25]. A similar trend is displayed by polythiophenes with alkyl side chains [20, 25, 26], which however tend to have a lower electrical conductivity than their counterparts with oligoether side chains (see Figure 1).

For some wearable applications where a good electrical conductor with a low stiffness is required, it would be advantageous to at least partially decouple the relationship between σ_{el} and E. Blending or complexation with a second polymer or reinforcing agent can be used to adjust the stiffness, which however tends to compromise σ_{el} (Figure 1) as the volume fraction of charge-conducting material is reduced unless the second component is itself a conductor [9, 27]. In case of PEDOT:PSS and PBFDO the addition of compounds that induce a plasticizing effect has yielded materials with a low $E \leq 0.1$ GPa without unduly reducing σ_{el} [28–30], with e.g., α-tocopherol synthesized PBFDO maintaining a value of about 1000 S cm^{-1} [30] (Figure 1). In a similar fashion, chemical dopants such as F_4TCNQ and the molybdenum dithiolene complex Mo(tfd-$COCF_3$)$_3$ have been found to act as a plasticizer for various polythiophenes, slightly reducing E upon oxidation compared to the neat polymer [26, 31, 32]. We have recently observed that doping of a polythiophene with increasing amounts of bistriflimidic acid (H-TFSI) first increases σ_{el} as well as E because of an oxidation-induced increase in crystalline order, while excessive doping led to a less ordered material with $\sigma_{el} = 58$ S cm^{-1} but a relatively low $E = 80$ MPa [21]. Besides plasticization and changes of the degree of order, other phenomena such as electrostatic interactions (e.g., those leading to ionic crosslinks), planarization of the conjugated backbone and changes in the glass transition temperature T_g can influence the rheological and mechanical properties [12, 25, 33–35]. Evidently, the selection of appropriate dopants or counterions may facilitate the design of conducting materials without resulting in an unduly high stiffness. While the comparison of doped polymers comprising different types of counterions has recently received considerable attention with regard to electrical transport [36–41], the effect on mechanical properties remains largely unexplored.

Here, we investigate how the electrical and mechanical properties of a thienothiophene copolymer with triethylene glycol side chains, p(g_3TT-T2), are affected by oxidizing the material using different processes (i.e., sequential doping or proton-coupled electron-transfer, PCET [42]; see Figure 2 for chemical structures and doping mechanisms), resulting in doped materials with comparable structural order but comprising different counterions. We chose p(g_3TT-T2) as a model system due to its promising electrical properties in conjunction with a low synthetic complexity, which eases the preparation of gram-scale batches that are needed for mechanical characterization [43, 44].

As a result, the conductivity of the polymer at room temperature can be controlled by the degree of oxidation of the polymer backbone. Materials with a similar $\sigma_{el} \approx 100$ S cm^{-1} feature significantly different elastic moduli with values varying from $E = 0.05$ to 0.7 GPa at room temperature, determined by the counterion-dependent ability of side chains to relax (Figure 1).

2 | Results and Discussion

All samples were prepared by casting the neat polymer from chloroform (8 g L^{-1}) solution, resulting in the same initial nanostructure in all cases, followed by sequential doping with acetonitrile solutions or PCET in the presence of an aqueous electrolyte. For sequential doping we chose F_4TCNQ, H-TFSI, and tris(4-bromophenyl) ammoniumyl hexachloroantimonate (Magic Blue) because all three compounds are known to strongly oxidize conjugated polymers while yielding different elastic moduli [20, 21]. Doping via PCET with *p*-benzoquinone (BQ) in the presence of LiNFSI allowed us to create a system with a larger counterion than TFSI and F_4TCNQ$^-$.

In an initial set of experiments, we used UV–vis-NIR spectroscopy to investigate the degree of oxidation of thin films of p(g_3TT-T2) that were either doped sequentially or via PCET with BQ in the presence of LiNFSI (Figure 3). Neat p(g_3TT-T2) features absorption bands in the visible region, with distinct peaks at 560 and 615 nm, which in case of, e.g., poly[2,5-bis(3-dodecylthiophen-2-yl)thieno(3,2-*b*)thiophene] (PBTTT) and poly(3-hexylthiophene) (P3HT) have been assigned to the presence of ordered domains [51–53]. The UV–vis-NIR absorption spectra of doped p(g_3TT-

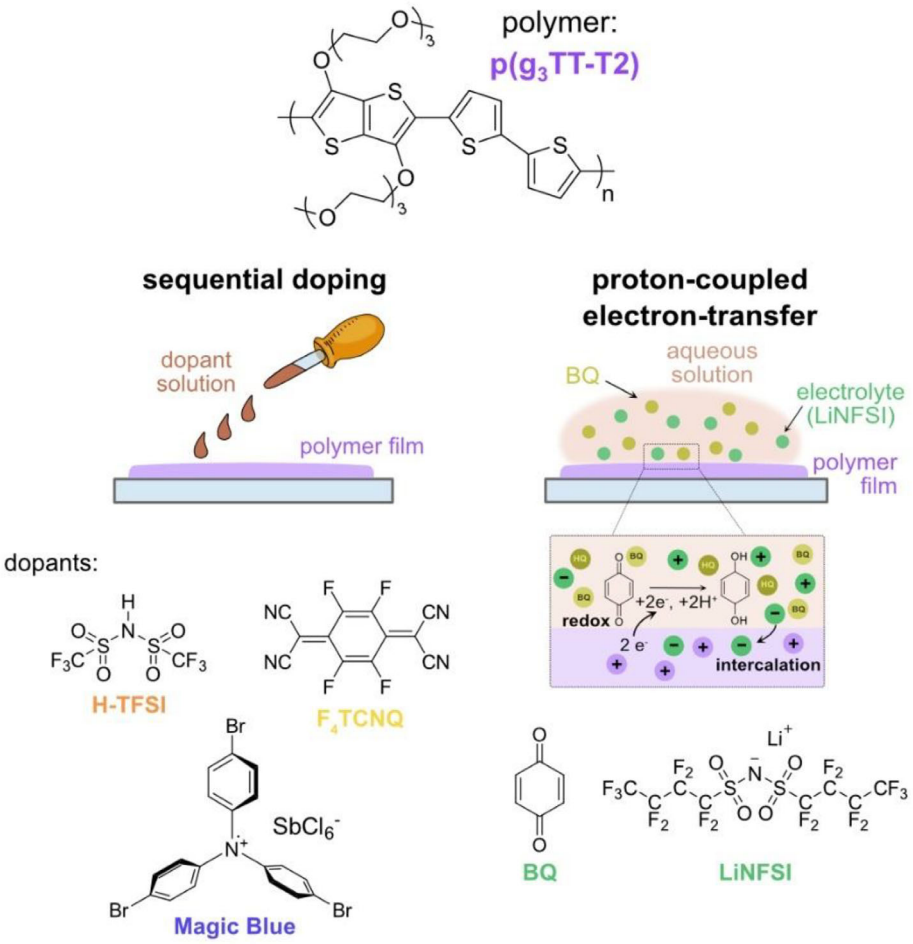

FIGURE 2 | Chemical structures of p(g_3TT-T2) and various dopant systems, as well as schematics illustrating sequential and proton-coupled electron-transfer (PCET) doping.

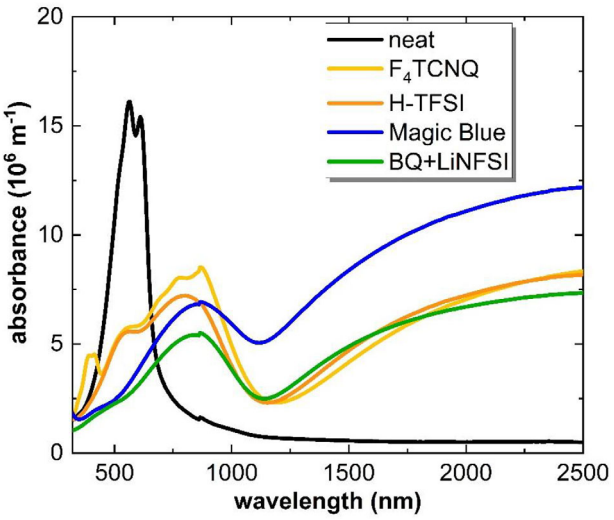

FIGURE 3 | UV–vis-NIR absorption spectra of neat and doped p(g_3TT-T2) with absorbance normalized by the sample thickness.

T2) indicate strong oxidation of the backbone in case of all doping mechanisms as evidenced by a decrease of the neat polymer absorption and the appearance of distinct polaronic absorption peaks in the NIR region. Two additional peaks around 800 nm are present in case of F_4TCNQ-doped p(g_3TT-T2), which are characteristic for F_4TCNQ anions [54]. Films doped via PCET with BQ in the presence of LiNFSI or sequentially doped with Magic Blue exhibit complete bleaching of the neat polymer absorption while F_4TCNQ- and H-TFSI-doped p(g_3TT-T2) retain a similar shoulder around 550 nm. This observation indicates a slightly higher degree of oxidation in case of Magic Blue and BQ-doped samples, while F_4TCNQ- and H-TFSI-doped films are less doped and feature a comparable oxidation level.

Knowledge about the oxidation level is critical for ensuring a fair comparison of films doped by different means. Therefore, we used X-ray photoemission spectroscopy (XPS) and quantitative ^{19}F nuclear magnetic resonance (^{19}F NMR) spectroscopy to estimate the charge-carrier density of doped p(g_3TT-T2) films (Figure 4). Both techniques enable direct quantification of the counterions within the film, allowing the estimation of the number of charge carriers, i.e., polarons, per unit volume N_p under the assumption that each dopant counterion corresponds to one polaron on the polymer backbone.

XPS enables the estimation of the molar ratio of atoms in each species, which is directly related to the ratio of peak integrals for a given transition. Since both p(g_3TT-T2) and some of the

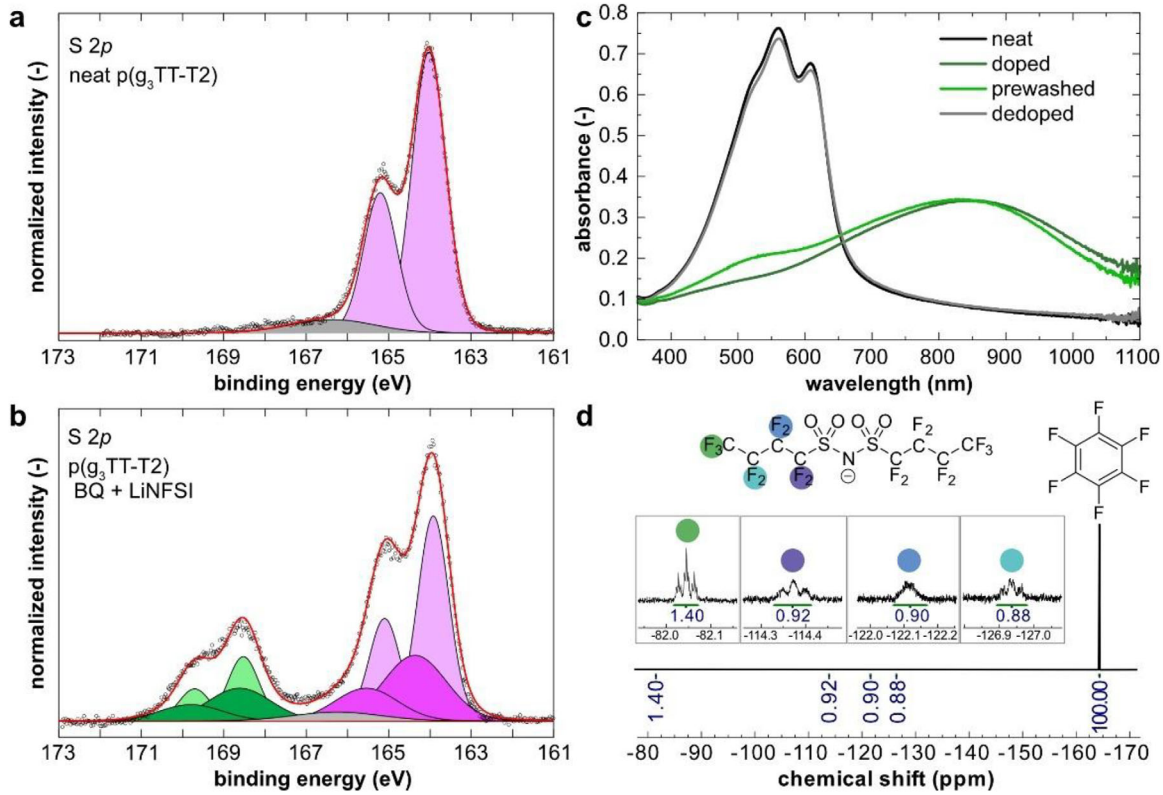

FIGURE 4 | a,b) Sulfur 2*p* XPS spectra of neat p(g_3TT-T2) and films doped via PCET with BQ in the presence of LiNFSI including peak fits corresponding to signals from neat polymer segments (light pink), chain segments with polarons (dark pink), and NFSI (green); c) UV–vis absorbance spectra of solid films of neat, doped, prewashed, and dedoped p(g_3TT-T2), and d) ^{19}F NMR spectra of NFSI and hexafluorobenzene solutions.

counterions, i.e., TFSI and NFSI, contain sulfur, the molar ratio of the anion to the polymer repeat unit can be determined by measuring the areas of the sulfur peaks corresponding to each component, as previously described by Jacobs et al. [39] XPS is a surface-sensitive technique. Hence, the method described here for the doped films works provided that the surface is representative of the whole sample, i.e., no doping gradients or unreacted dopant are present. To remove residual electrolyte and dopant from the film surface, we added a washing step to the doping process prior to XPS measurements (see Experimental Section). For the peak fitting, separate 2*p* doublet components were assigned to neutral polymer chain segments and those with polarons (Figure 4a), with the latter being shifted to a higher binding energy due to the positive charge (see Supporting Information for details). Distinct 2*p* doublet components were used to describe the peaks arising for NFSI or TFSI due to the different spatial environment of the two sulfur atoms as described by Jacobs et al. [39] (Figure 4a).

The comparison of the peak areas allowed to determine the molar ratio of counterions or dopants to polymer repeat units yielding values of $x_{d,XPS} = 0.67 \pm 0.07$ and $x_{d,XPS} = 0.76 \pm 0.08$ for films doped with H-TFSI and via PCET with BQ in the presence of LiNFSI, respectively (see Supporting Information and Figure S1). Instead, for films doped with Magic Blue and F_4TCNQ, which both lack sulfur atoms, the molar ratio of dopant to polymer repeat unit was estimated using the 2*p* doublet peaks attributed to neutral polymer segments and those with polarons (Figure S1; see Supporting Information for details). Thus, values of $x_{d,XPS} = 0.74 \pm 0.08$ and 0.50 ± 0.05 were obtained for Magic Blue and F_4TCNQ doped films, respectively.

We then estimated the number of charge-carriers per doped-film volume N_p^{XPS}, assuming that each dopant counterion corresponds to one polaron on the polymer backbone (see Supporting Information and Equation S2 for details). The resulting values for the charge-carrier density N_p^{XPS} ranged from $(0.34 \pm 0.08) \cdot 10^{27}$ m^{-3} to $(0.96 \pm 0.15) \cdot 10^{27}$ m^{-3} for F_4TCNQ-and Magic Blue-doped p(g_3TT-T2), respectively (Table 1). The values obtained for H-TFSI and F_4TCNQ doped films are lower than those doped with Magic Blue and BQ + LiNFSI, which is consistent with the higher doping level of the latter two systems inferred from UV–vis spectra (see Figure 3).

We employed ^{19}F NMR to validate the charge-carrier density estimated by XPS (see Supporting Information for details). This could confidently be done only for BQ-doped p(g_3TT-T2), given its higher doping level compared to F_4TCNQ- and H-TFSI-doped films. Moreover, ^{19}F NMR of F_4TCNQ is non-trivial given its long relaxation time [55, 56]. ^{19}F NMR allows for the measurement of the absolute concentration of fluorine atoms by integrating the NMR signals of the target species and comparing them to that of an internal standard, in our case hexafluorobenzene, of known concentration. The integrated intensity ratios of each signal in a ^{19}F NMR spectrum are proportional to the mole ratio of the corresponding nuclei. NFSI counterions were removed from the doped thin films by dedoping the sample using triethylamine in deuterated acetonitrile solution, as previously described

TABLE 1 | Composition of doped films: molar ratio of counterions or dopants to polymer repeat unit $x_{d,XPS}$ from XPS (error of 10% based on uncertainty in fitting), ionization efficiency η_{ion} (error of 15% based on uncertainty in fitting), thickness of thin films before and after doping, d_n and d_d (mean and standard deviation of 5 measurements), swelling ratio d_d/d_n (error derived from error propagation), density of doped films ρ_d (error derived from error propagation; c.f. Equation S3), and number of charge carriers per unit volume from XPS, N_p^{XPS} (error derived from error propagation; cf. Equation S2 for calculation of N_p^{XPS} based on $x_{d,XPS}$, η_{ion}, d_d/d_n and the density of a neat polymer film $\rho_n = (1.22 \pm 0.05)$ g cm^{-3}; see Supporting Information).

Dopant	$x_{d,XPS}$ (−)	η_{ion} (%)	d_n (nm)	d_d (nm)	d_d/d_n (−)	ρ_d (g cm^{-3})	N_p^{XPS} (10^{27} m^{-3})
H-TFSI	0.67 ± 0.07	47 ± 5	37 ± 4	33 ± 4	0.9 ± 0.1	1.76 ± 0.22	0.41 ± 0.07
BQ + LiNFSI	0.76 ± 0.08	100	28 ± 3	34 ± 2	1.2 ± 0.1	1.73 ± 0.18	0.74 ± 0.10
Magic Blue	0.74 ± 0.08	100	39 ± 2	35 ± 3	0.9 ± 0.1	1.89 ± 0.25	0.96 ± 0.15
F_4TCNQ	0.50 ± 0.05	63 ± 7	38 ± 3	40 ± 5	1.1 ± 0.2	1.35 ± 0.26	0.34 ± 0.08

TABLE 2 | Electrical properties of doped p(g_3TT-T2) films: charge-carrier density N_p^{XPS} from XPS measurements, electrical conductivity σ_{el} (mean and standard deviation of five measurements on the same sample are given), Seebeck coefficient α (mean and standard deviation of five measurements on the same sample) and charge-carrier mobility μ (error derived from error propagation; cf Equation (1)).

Dopant	N_p^{XPS} (10^{27} m^{-3})	σ_{el} (S cm^{-1})	α (μV K^{-1})	μ (cm^2 V^{-1} s^{-1})
H-TFSI	0.41 ± 0.07	117 ± 42	21 ± 2	1.8 ± 0.7
BQ + LiNFSI	0.74 ± 0.10	125 ± 22	18 ± 2	1.1 ± 0.2
Magic Blue	0.96 ± 0.12	188 ± 6	12 ± 1	1.2 ± 0.2
F_4TCNQ	0.34 ± 0.08	104 ± 19	27 ± 2	1.9 ± 0.6

[39, 57]. ^{19}F NMR spectra of samples composed of dedoping solution and hexafluorobenzene stock solution were recorded (Figure 4). UV–vis spectra were measured to verify that films were largely dedoped, as evidenced by the almost complete recovery of the neutral absorption bands of the polymer in the visible region (Figure 4). The charge-carrier density was estimated by dividing the NFSI concentration obtained from integration of NMR spectra by the dry volume of the neat film multiplied by the swelling ratio d_d/d_n. The estimated number of polarons per unit volume is approximately $N_p^{NMR} = (1.06 \pm 0.21) \cdot 10^{27}$ m^{-3} (the error was given a value of 20% to account for uncertainties in the volume measurements of the thin film), which is similar to the value obtained by XPS. Differences may arise because XPS can be accompanied by beam-induced de-doping or loss of dopant due to extended exposure to vacuum (see Supporting Information and Figure S3).

We then explored the electrical properties of doped p(g_3TT-T2) films (Table 2). All doping mechanisms result in a high electrical conductivity exceeding 100 S cm^{-1}, with values ranging from σ_{el} = (104 ± 19) S cm^{-1} in case of F_4TCNQ to (188 ± 6) S cm^{-1} for Magic Blue-doped p(g_3TT-T2). Using the obtained values for σ_{el} and N_p^{XPS}, we were able to estimate the charge-carrier mobility μ for the doped p(g_3TT-T2) samples according to:

$$\sigma_{el} = N_p^{XPS} \cdot \mu \cdot e \quad (1)$$

where e is the elementary charge. We obtain values ranging from of $\mu = (1.1 \pm 0.2)$ cm^2 V^{-1} s^{-1} for BQ-doped p(g_3TT-T2) to $\mu = (1.9 \pm 0.6)$ cm^2 V^{-1} s^{-1} for F_4TCNQ-doped p(g_3TT-T2).

The Seebeck coefficient α is similar for all samples with values ranging from 12 to 27 μV K^{-1}, with lower values in case of Magic Blue and BQ-doped films (Table 2), which is in agreement with the somewhat higher oxidation level inferred from UV–vis-NIR spectra (Figure 3) and the estimated charge-carrier density (Table 1).

Grazing-incidence wide-angle X-ray scattering (GIWAXS) was carried out to determine the impact of the doping mechanism on the degree of order of p(g_3TT-T2) films (see Figure S4 for GIWAXS 2D patterns). GIWAXS diffractograms obtained for the neat polymer revealed that p(g_3TT-T2) exhibits a high degree of solid-state order and a predominant edge-on texture, as indicated by the out-of-plane $h00$ diffraction peaks, at $q_{100} \approx 4.2$ nm^{-1}, $q_{200} \approx 8.4$ nm^{-1} and $q_{300} \approx 12.5$ nm^{-1}, along with an in-plane q_{010} diffraction at about 17.1 nm^{-1}, characteristic of π-stacking (Figure 5). All doped films retain a high degree of order and an edge-on texture. The out-of-plane $h00$ diffraction peaks and the in-plane q_{010} diffraction shift to lower and higher q values, respectively, suggesting that doping induces an expansion along the side-chain stacking direction and a contraction of the π-stacking distance. The distance between scattering planes in the lamellar direction increases from $d_{100} = 2\pi/q_{100} = 14.8$ Å in case of the neat polymer to a value of 16.5, 17.7, 17.9, and 21.5 Å for samples doped with Magic Blue, F_4TCNQ, H-TFSI, and BQ (with NFSI as the counterion), respectively, which is consistent with intercalation of dopant counterions between the side chains in ordered domains. The increase in lamellar spacing d_{100} correlates with the Van der Waals volume of the counterions, computed according to an empirical relationship proposed by Zhao et al.

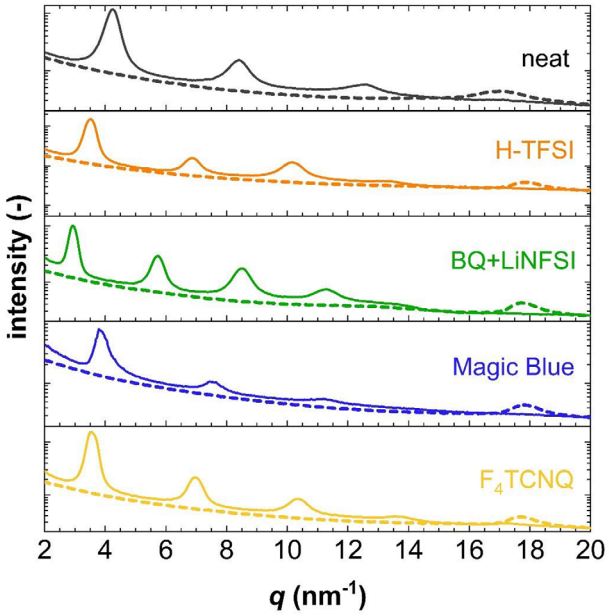

FIGURE 5 | In-plane (dashed line) and out-of-plane (solid line) GIWAXS diffractograms of neat and doped p(g_3TT-T2) films.

[58] that considers the types of atoms as well as the number of bonds and aromatic rings (Figure S5). This observation suggests that intercalation of larger counterions also results in a larger expansion of the unit cell along the side-chain stacking direction.

After characterizing the optoelectronic properties and the microstructure of neat and doped p(g_3TT-T2), we determined their mechanical properties. We performed dynamic mechanical thermal analysis (DMTA) of neat and doped p(g_3TT-T2) to investigate how the presence of counterions influences the relaxation processes of the material. DMTA in tensile mode at a frequency of 1 Hz of a 200 μm thick free-standing sample of neat p(g_3TT-T2), processed via solid-state compression molding at 180°C, revealed two distinct transitions upon heating the material from −80°C to 60°C (Figure 6a), suggesting the occurrence of two distinguishable relaxation processes. A first sub-glass transition T_β is observed at −50°C, as evidenced by a decrease in storage modulus E' from above to below 1 GPa, along with peaks in loss modulus E'' and tan δ. This transition is likely associated with relaxation of the triethylene glycol side chains, given the similar low glass transition temperature $T_g = -50$°C reported for poly(ethylene oxide) (PEO) [59]. A second transition appears at T_α of −5°C as evidenced by a further peak in tan δ. This transition is attributed to main-chain (polymer backbone) relaxation, i.e., the T_g.

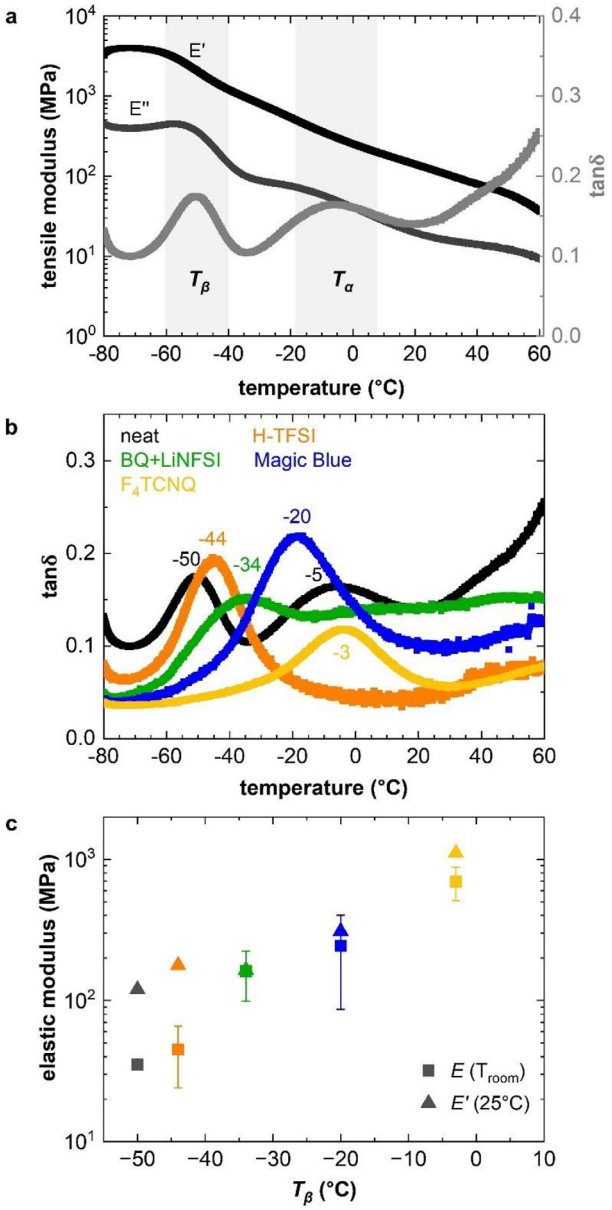

FIGURE 6 | a) Dynamic mechanical thermal analysis (DMTA) thermograms showing the tensile storage modulus E', loss modulus E'', and tan δ of a free-standing film of neat p(g_3TT-T2); b) tan δ of free-standing films of neat and doped p(g_3TT-T2); and c) tensile elastic modulus at room temperature versus the sub-glass transition temperature T_β inferred from the peak in tan δ; Young's modulus E at room temperature (squares) and tensile storage modulus E' at 25°C (triangles) from tensile deformation and DMTA, respectively (data points and error bars correspond to the mean and standard deviation of 3–4 measurements of different samples).

We doped 50–100 μm thick free-standing samples using the same procedures as those utilized for thin films. A comparison of the masses of the neat and doped samples (Table S1) and the optical images of their surface (Figure S6) confirmed that the samples were strongly doped. DMTA thermographs of doped p(g_3TT-T2) show a single transition (Figure 6b and Figure S7), as indicated by a single peak in tan δ, which is at a different location compared with those observed for the neat polymer, confirming that films are doped throughout (inhomogeneous doping with an undoped central part would lead to the presence of two tan δ peaks from the neat and doped polymer, respectively). This suggests that only one dominant or, alternatively, two overlapping relaxation processes occur within the temperature range of −80°C to 60°C. Notably, regardless of the doping mechanism the observed tan δ peak shifts to higher temperatures. We argue that this peak in tan δ is associated with side-chain relaxation since no other transition is apparent at lower temperatures where $E' > 1$ GPa. The backbone relaxation, instead, has likely shifted to substantially higher temperatures outside the measured temperature interval, similar to the absence of a detectable T_g in case of dry polyelectrolyte

complexes [60]. A comparison of undoped and doped films shows that the extent of the shift in the tan δ peak varies with the type of counterion (Figure 6b). For instance, in case of H-TFSI-doped p(g_3TT-T2), T_β only increased slightly to −44°C, i.e., just 6°C higher than T_β of the neat polymer at −50°C. A more substantial increase is observed for BQ- and Magic Blue-doped samples, where T_β reached −34°C and −20°C, respectively. The most pronounced increase is found in case of p(g_3TT-T2) doped with F_4TCNQ with T_β reaching a value of −3°C.

Given the differences in the relaxation temperatures T_β of doped p(g_3TT-T2), we investigated whether variations in free volume available for side-chain relaxation or differences in density could account for the observed results. Compared to the other doped films, F_4TCNQ-doped films feature the highest T_β, but a significantly lower density of $\rho_d = (1.35 \pm 0.26)$ g cm^{-3} (Table 1) and thus a higher fractional free volume, which inversely scales with density. Therefore, we argue that differences in the free volume available for side-chain relaxation are unlikely to account for the differences in T_β since the films with the lowest density, i.e., F_4TCNQ-doped films, should also feature the lowest transition temperature.

It is feasible that the observed differences in T_β arise because of an uneven (heterogeneous) distribution of counterions within the polymer matrix, which likely reside in both ordered and disordered domains. The distribution of counterions can be influenced by a number of factors including the overall concentration (which is similar for the investigated samples; see Table 1), processing parameters such as the type of solvent and the means of counterion insertion, electrostatic interactions and the miscibility between the dopant and the polymer [61–63], which can lead to clustering [64, 65] or preferential localization in specific (ordered or disordered) regions [66, 67]. Ultimately, since low-temperature relaxation processes in polymers typically occur in disordered domains, the amount and distribution of counterions within the latter can be anticipated to influence T_β. Interestingly, PEO blended with $LiClO_4$ has been found to first feature a strong increase in the T_g with salt concentration followed by a return to a value similar to the T_g of the neat polymer, which has been explained with phase separation into polymer- and salt-rich domains [68, 69]. In analogy with PEO salt mixtures, we tentatively assign the lower T_β values observed for H-TFSI- and BQ-doped p(g_3TT-T2) to the presence of polymer-rich disordered domains, which may arise either because of the presence of clusters of counterions or because ordered domains take up a larger fraction of the counterions compared to Magic Blue- and F_4TCNQ-doped samples. In contrast, Magic Blue- and F_4TCNQ-doped samples are expected to feature disordered domains that comprise a larger fraction of counterions, leading to a higher T_β (note that GIWAXS indicates that ordered domains in all investigated systems take up counterions; see Figure 5).

In a final set of experiments, we investigated the mechanical properties of p(g_3TT-T2) in both its neat and oxidized states using tensile deformation at room temperature (Figure 7a and Figures S8–S12). The neat polymer exhibits a Young's modulus of $E = (35 \pm 2)$ MPa and an elongation at break of $\varepsilon_{break} = (4.7 \pm 1.1)$%, indicating a relatively soft but brittle material. Upon doping, the polymer becomes stiffer, as evidenced by an increase in E, ranging from $E = 0.05$ to 0.7 GPa, and a decrease in ε_{break}.

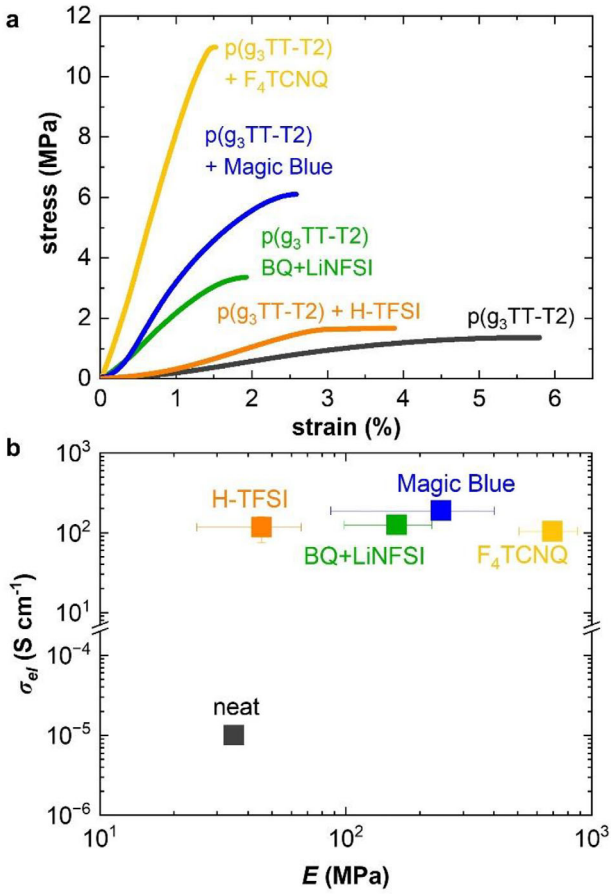

FIGURE 7 | a) Representative stress-strain tensile deformation curves of free-standing films of neat and doped p(g_3TT-T2) recorded at room temperature; b) electrical conductivity σ_{el} vs. Young's modulus E of neat and doped p(g_3TT-T2) (data points and error bars correspond to the mean and standard deviation of 5 measurements on the same sample for σ_{el} and 3–4 measurements of different samples for E).

Interestingly, tensile elastic modulus values at room temperature obtained from both DMTA and tensile deformation increase with T_β (Figure 6c). For instance, H-TFSI-doped p(g_3TT-T2) showed the least increase in both T_β and Young's modulus, with $E = (45 \pm 21)$ MPa (Figure S11). A more substantial increase in Young's modulus was observed for BQ- and Magic Blue-doped samples, with $E = (162 \pm 63)$ MPa (Figure S9) and $E = (244 \pm 157)$ MPa (Figure S12), respectively. The largest Young's modulus with $E = (693 \pm 185)$ MPa (Figure S10) was found in case of F_4TCNQ-doped p(g_3TT-T2), which exhibits also the highest T_β among the doped samples. We assign the relatively large variation in the Young's moduli of each set of tensile-drawn doped samples to challenges with regard to sample handling after doping and clamping in the dynamic mechanical analyzer (DMA) instrument, rather than to intrinsic differences between samples (cf. large error bars of tensile-drawn doped samples in Figure 6c). We conclude that the stiffness at room temperature of p(g_3TT-T2) correlates with T_β and thus depends on the ability of side chains to relax.

Doped p(g_3TT-T2) films with different counterions feature a similar $\sigma_{el} \approx 100$ S cm^{-1}, but a significantly different Young's modulus at room temperature (Figure 7b). This suggests that the electrical conductivity is determined by the degree of oxidation of

the polymer backbone, while the stiffness at room temperature is determined by the ability of side chains to relax, which we tentatively assign to differences in the distribution of counterions, varying with the type of dopant counterion (and, potentially, doping method). As a result, selecting a specific doping mechanism and dopant counterion allows to partially decouple the often-observed correlation between σ_{el} and E (c.f. Figure 1).

3 | Conclusions

Sequential doping and PCET were used to prepare p(g_3TT-T2) films that comprised different counterions but featured a comparable oxidation level and consequently electrical conductivity, with values above 100 S cm^{-1}. GIWAXS indicated that doping leads to an expansion of the lamellar distance of ordered domains, along with a reduction in the π-stacking distance, which we explain with intercalation of the counterions between the triethylene glycol side chains in ordered domains. Doping leads to a counterion-dependent increase in the side-chain relaxation temperature T_β, which ranged from $T_\beta = -44°C$ to $-3°C$ for doped films despite a similar oxidation level. The Young's modulus of doped p(g_3TT-T2), which is strongly influenced by T_β, varied from 0.05 to 0.7 GPa at room temperature depending on the type of counterion. It can be concluded that the selection of appropriate dopant counterions (and doping processes) may provide a tool to modulate the mechanical properties of selected conducting polymers without significantly impacting their electrical performance. This partial decoupling of the electrical and mechanical properties, which are governed by the backbone and side-chain regions, respectively, may aid the design of soft conductors and more sustainable bioelectronic and wearable devices whose various soft and rigid components could be manufactured with the same polymer. Future studies that investigate the effect of molecular weight, side-chain length, and different conjugated backbones would be valuable for providing further insight into how the partial decoupling between electrical and mechanical properties extends to other systems and for guiding material design. Moreover, it is recommended that future studies include mechanical measurements on thinner samples, e.g., by employing atomic force microscopy (AFM), nanoindentation, or tensile testing on a liquid interface.

4 | Experimental Section

4.1 | Materials

P(g_3TT-T2) (number-average molecular weight determined by NMR or size exclusion chromatograph (SEC), $M_{n,NMR}$ = 9 kg mol^{-1} and $M_{n,SEC}$ = 13 kg mol^{-1}, and dispersity $Đ$ = 1.5 from SEC) was synthesized according to reported procedures [43]. 2,3,5,6-Tetrafluoro-7,7,8,8-tetracyanoquinodimethane (F_4TCNQ, purity >98%), lithium bis(nonafluorobutanesulfonyl)imide (LiN-FSI, purity >95%), and bistriflimidic acid (H-TFSI, purity >98%) were purchased from Tokyo Chemical Industry (TCI) and used as received. *p*-Benzoquinone (BQ, purity ≥98%), tris(4-bromophenyl) ammoniumyl hexachloroantimonate (Magic Blue, technical grade), chloroform ($CHCl_3$, purity >99.8%), acetonitrile (AcN, purity >99.9%), acetonitrile-d_3 (AcN-d_3, purity ≥99.8%), triethylamine (TEA, purity ≥99.5%) and buffer aqueous solutions at pH = 2 containing citric acid, sodium hydroxide and hydrogen chloride were purchased from Sigma Aldrich and used as received. Hexafluorobenzene (purity >98%) was purchased from Combi-Blocks. Extra dry acetonitrile (AcN, purity 99.9%) was purchased from Fisher Scientific.

4.2 | Sample Preparation

Thin films were prepared by spin coating (1000–1500 rpm for 60 s, 500 rpm s^{-1}) or blade coating a solution of the polymer in degassed $CHCl_3$ (8 g L^{-1}) onto precleaned microscopy glass slides for UV–vis spectroscopy, electrical characterization, determination of the density and charge-carrier density, polyethylene terephthalate (PET) sheets for Seebeck measurements, or cut silicon wafers for GIWAXS. The polymer thin films were annealed at 80°C for 15 min and then doped by adding the dopant solution on the surface or by dipping the sample in the dopant solution for 5 min. The dopant solutions were made by dissolving the dopant agent in the respective solvent with the concentrations reported in Table 3.

Free-standing samples with a thickness of 50–200 µm for mechanical testing were hot pressed at 180°C for 5 min between two Kapton sheets precoated with a sacrificial layer (NaPSS in MilliQ water at 50 g L^{-1}). The hot-pressed films were peeled off from the Kapton sheets by immersing them in deionized water allowing the dissolution of the sacrificial layer, followed by drying at 40°C under vacuum overnight (13–15 h). The free-standing films were doped by dipping them in the dopant solution (see Table 3 for dopant solution composition) for 4 h in case of F_4TCNQ, Magic Blue, and H-TFSI and 24 h for PCET doping, followed by drying at 40°C under vacuum overnight (13–15 h). A (0.56 ± 0.02) mm thick free-standing film for density measurements was hot pressed at 120°C for 10 min between two Teflon sheets.

4.3 | Grazing-Incidence Wide-Angle X-Ray Scattering (GIWAXS)

Films were prepared by spin-coating the polymer solution onto cleaned (by sonication in acetone and then in isopropanol, and spin-coated at 3000 rpm with toluene) silicon wafers and sequential doping. GIWAXS diffractograms were recorded at the beamline NCD – SWEET of the Alba synchrotron light source facility using an X-ray wavelength of 1 Å and a sample-detector distance of 201.17 cm.

4.4 | UV–Vis Absorption Spectroscopy

A PerkinElmer Lambda 1050 or an Agilent Technologies Cary 60 spectrophotometer were used to record UV–vis-NIR spectra on thin films with a thickness of 25–90 nm.

4.5 | Electrical Characterization

The electrical resistance of thin films was measured using a four-point probe set-up from Jandel Engineering (cylindrical probe head, RM3000) using collinear tungsten carbide electrodes at regular spacing of 1 mm. The thickness of thin films was mea-

TABLE 3 | Composition of dopant solutions describing the solvent and concentration of components.

DOPANT	SOLVENT	DOPANT CONCENTRATION
F_4TCNQ	degassed AcN	2.7 g L^{-1} (10 mM)
H-TFSI	degassed AcN	2.8 g L^{-1} (10 mM) + thermal activation at 80°C
Magic Blue	extra dry AcN	0.5 g L^{-1}
PCET: BQ + LiNFSI	aqueous buffer solution at pH = 2	BQ (2.7 g L^{-1}, 25 mM), LiNFSI (0.6 g L^{-1}, 1 mM)

sured by mechanical (KLA Tencor D100) or optical profilometry (Sensofar S neox). The electrical resistance of thick samples, fixated with silver paint from Agar Scientific Ltd on a glass slide, was measured in two-point configuration using a Keithley 2400 source-measure unit. The Seebeck coefficient was measured by an SB1000 instrument (MMR Technologies) equipped with a K2000 temperature controller (MMR Technologies) using a thermal load of 1–2 K and a constantan wire as internal reference. Films were prepared by spin coating on PET foil, then doped and finally cut into pieces of around 1 × 5 mm. Mounting on a SB1000 sample stage was done with carbon paint (DAG-T-502, Ted Pella) for Magic Blue-doped samples and silver paint (fast-drying silver suspension from Agar Scientific Ltd) for all the other doped polymer films.

4.6 | Quantitative ^{19}F NMR

P(g_3TT-T2) thin films were spin-coated onto pre-cleaned glass slides and then doped via PCET with BQ using LiNFSI as the electrolyte according to Table 3. The outer part of the film was removed to obtain a square film with an area of (1.4 ± 0.2) cm^2 and a uniform thickness. The films were dedoped using 2 mL of a 10% v:v TEA in AcN-d_3 solution in a closed container to prevent evaporation. After 5 min of dedoping, 0.7 mL of the solution was added to an NMR tube together with 20 µL of 25.5 mM of hexafluorobenzene in AcN-d_3, used as ^{19}F QNMR reference compound (600 MHz, C_6F_6: $\delta(^{19}F) = -164.9$ ppm). NMR spectra were recorded on a Bruker Avance NEO 600 spectrometer (^{19}F: 564.3 MHz). An O1 transmitter frequency of −125.0 ppm was chosen with a spectral width of 100 ppm. For each sample, 24 scans with a D1 relaxation delay time of 30 s was chosen to ascertain proper relaxation of the compounds between scans. Acquired spectra were analyzed using MestReNova software, using a polynomial fit baseline correction (order 20, 0.11 Hz) between −79.0 ppm and −169.0 ppm.

4.7 | X-Ray Photoemission Spectroscopy (XPS)

P(g_3TT-T2) thin films were spin-coated onto pre-cleaned glass slides with an area of 1 cm^2 and then doped according to Table 3. Residual dopant and/or electrolyte on the surface was removed by rinsing with acetonitrile or deionized water via spin-coating (3000 rpm). The XPS spectra were recorded on a Versaprobe III scanning XPS system (Physical Instruments) using monochromatized Al-Kα radiation with an illuminated spot size of 100 µm^2. The samples were mounted on a non-conductive adhesive. Charge compensation was ensured by a combination of an electron flood gun and an Ar^+ ion source. The binding energy scale was referenced to the leading peak in the carbon 1*s* spectra, which originates from the long side chains of p(g_3TT-T2) containing C—O bonds for which we assume a typical position of 286.4 eV (Figure S13) [70]. The S 2*p* spectra were recorded with a step width of 0.025 eV at a pass energy of 13 eV; all other spectra with 26 eV pass energy and 0.05 eV step width. The S 2*p* spectra were decomposed by a set of Voigt profiles after subtracting a Shirley-type background. The full width at half maximum (FWHM) for the Lorentzian and Gaussian part were treated separately. The Lorentzian widths for the S 2*p* signals were fixed to 0.09 eV [71]. The Gaussian widths were allowed to vary with the constraint of being of same value for spin-orbit split signals. The S 2*p* spectra were fitted with spin-orbit split doublets with a separation of 1.18 eV for the $2p_{3/2}$ and $2p_{1/2}$ components [72].

4.8 | Density Measurements

The mass m_n and volume V_n of a (0.56 ± 0.02) mm thick free-standing p(g_3TT-T2) film was determined using a XS105 scale from Mettler Toledo and a vernier caliper, respectively. To determine the density of doped samples, the thickness of 30–40 nm thin films was measured before and after doping with optical interferometry using a Sensofar S neox 3D optical profilometer.

4.9 | Dynamic Mechanical Thermal Analysis (DMTA) and Tensile Testing

Dynamic mechanical thermal analysis (DMTA) of free-standing samples was performed using a Discovery 850 dynamic mechanical analyzer (DMA) from TA Instruments. A preload force of 0.005–0.01 N was used when mounting samples and an oscillating strain of 0.02–0.05% at a frequency of 1 Hz was applied while ramping the temperature from −80°C to 100°C at a rate of 3°C min^{-1}. Tensile testing of free-standing samples was performed using a Q800 dynamic mechanical analyzer (DMA) from TA Instruments at room temperature in controlled force mode with a force rate of 0.005 N min^{-1} using a preload force of 0.001 N and gauge length of 3.7–4.2 mm.

4.10 | Statistical Analysis

All data were used as obtained from the various instruments. There was no removal of outliers. All raw data are published in Zenodo. All thickness, electrical conductivity, Seebeck coefficient, and Young's modulus values correspond to the mean and

standard deviation with the sample size stated in the relevant figure or table legends.

Acknowledgements

The authors gratefully acknowledge financial support from the European Union's Horizon 2020 research and innovation programme through the Marie Skłodowska-Curie grant agreement no. 955837 (HORATES), from the European Research Council (ERC) under grant agreement no. 101043417, from the Knut and Alice Wallenberg Foundation (2020.0187 and 2022.0034), and from the ICIU/AEI/10.13039/501100011033 for the "Severo Ochoa" program for Centres of Excellence CEX2023-001263-S. We thank Eric Tam from the Department of Industrial Materials Science at Chalmers for technical support of the XPS measurements. GIWAXS experiments were performed at the NCD-SWEET beamline of the ALBA Synchrotron with the collaboration of ALBA staff.

Conflicts of Interest

The authors declare no conflicts of interest.

Data Availability Statement

The data that support the findings of this study are openly available in Zenodo at https://doi.org/10.5281/zenodo.17184539.

References

1. Z. Wang, D. Zhang, L. Yang, et al., "Mechanically Robust and Stretchable Organic Solar Cells Plasticized by Small-Molecule Acceptors," *Science* 387, no. 6732 (2025): 381–387, https://doi.org/10.1126/science.adp9709.

2. S. Zokaei, M. Craighero, C. Cea, et al., "Electrically Conducting Elastomeric Fibers with High Stretchability and Stability," *Small* 18, no. 5 (2022): 2102813, https://doi.org/10.1002/smll.202102813.

3. L. V. Kayser and D. J. Lipomi, "Stretchable Conductive Polymers and Composites Based on PEDOT and PEDOT:PSS," *Advanced Materials* 31, no. 10 (2019): 1806133, https://doi.org/10.1002/adma.201806133.

4. T. R. Ray, J. Choi, A. J. Bandodkar, et al., "Bio-Integrated Wearable Systems: a Comprehensive Review," *Chemical Reviews* 119, no. 8 (2019): 5461–5533, https://doi.org/10.1021/acs.chemrev.8b00573.

5. M. Craighero, Q. Li, Z. Zeng, et al., "Poly(benzodifurandione) Coated Silk Yarn for Thermoelectric Textiles," *Advanced Science* 11, no. 38 (2024): 2406770, https://doi.org/10.1002/advs.202406770.

6. J. Mun, Y. Ochiai, W. Wang, et al., "A Design Strategy for High Mobility Stretchable Polymer Semiconductors," *Nature Communications* 12, no. 1 (2021): 3572, https://doi.org/10.1038/s41467-021-23798-2.

7. S. Inal, J. Rivnay, A.-O. Suiu, G. G. Malliaras, and I. McCulloch, "Conjugated Polymers in Bioelectronics," *Accounts of Chemical Research* 51, no. 6 (2018): 1368–1376, https://doi.org/10.1021/acs.accounts.7b00624.

8. G. Malliaras and I. McCulloch, "Introduction: Organic Bioelectronics," *Chemical Reviews* 122, no. 4 (2022): 4323–4324, https://doi.org/10.1021/acs.chemrev.2c00026.

9. A. Lund, Y. Wu, B. Fenech-Salerno, F. Torrisi, T. B. Carmichael, and C. Müller, "Conducting Materials as Building Blocks for Electronic Textiles," *MRS Bulletin* 46, no. 6 (2021): 491–501, https://doi.org/10.1557/s43577-021-00117-0.

10. R. Kroon, D. A. Mengistie, D. Kiefer, et al., "Thermoelectric Plastics: from Design to Synthesis, Processing and Structure–Property Relationships," *Chemical Society Reviews* 45, no. 22 (2016): 6147–6164, https://doi.org/10.1039/C6CS00149A.

11. N. Pataki, P. Rossi, and M. Caironi, "Solution Processed Organic Thermoelectric Generators as Energy Harvesters for the Internet of Things," *Applied Physics Letters* 121 (2022): 230501, https://doi.org/10.1063/5.0129861.

12. S. H. K. Paleti, Y. Kim, J. Kimpel, M. Craighero, S. Haraguchi, and C. Müller, "Impact of Doping on the Mechanical Properties of Conjugated Polymers," *Chemical Society Reviews* 53, no. 4 (2024): 1702–1729, https://doi.org/10.1039/D3CS00833A.

13. N. Dowling, S. Kampe, and M. Kral, *Mechanical Behavior of Materials* (Pearson Education Limited, 2007), 992.

14. S. Zokaei, R. Kroon, J. Gladisch, et al., "Toughening of a Soft Polar Polythiophene through Copolymerization with Hard Urethane Segments," *Advanced Science* 8, no. 2 (2021): 2002778, https://doi.org/10.1002/advs.202002778.

15. M. Ashizawa, Y. Zheng, H. Tran, and Z. Bao, "Intrinsically Stretchable Conjugated Polymer Semiconductors in Field Effect Transistors," *Progress in Polymer Science* 100 (2020): 101181, https://doi.org/10.1016/j.progpolymsci.2019.101181.

16. M. Z. Seyedin, J. M. Razal, P. C. Innis, and G. G. Wallace, "Strain-Responsive Polyurethane/PEDOT:PSS Elastomeric Composite Fibers with High Electrical Conductivity," *Advanced Functional Materials* 24, no. 20 (2014): 2957–2966, https://doi.org/10.1002/adfm.201303905.

17. D. Kiefer, L. Yu, E. Fransson, et al., "A Solution-Doped Polymer Semiconductor: Insulator Blend for Thermoelectrics," *Advanced Science* 4, no. 1 (2017): 1600203, https://doi.org/10.1002/advs.201600203.

18. M. Mone, Y. Kim, S. Darabi, et al., "Mechanically Adaptive Mixed Ionic-Electronic Conductors Based on a Polar Polythiophene Reinforced with Cellulose Nanofibrils," *ACS Applied Materials & Interfaces* 15, no. 23 (2023): 28300–28309, https://doi.org/10.1021/acsami.3c03962.

19. D. Zhao, Q. Zhang, W. Chen, et al., "Highly Flexible and Conductive Cellulose-Mediated PEDOT:PSS/MWCNT Composite Films for Supercapacitor Electrodes," *ACS Applied Materials & Interfaces* 9, no. 15 (2017): 13213–13222, https://doi.org/10.1021/acsami.7b01852.

20. S. Zokaei, D. Kim, E. Järsvall, et al., "Tuning of the Elastic Modulus of a Soft Polythiophene through Molecular Doping," *Materials Horizons* 9, no. 1 (2022): 433–443, https://doi.org/10.1039/D1MH01079D.

21. S. Hultmark, M. Craighero, S. Zokaei, et al., "Impact of Oxidation-Induced Ordering on the Electrical and Mechanical Properties of a Polythiophene Co-Processed with Bistriflimidic Acid," *Journal of Materials Chemistry C* 11, no. 24 (2023): 8091–8099, https://doi.org/10.1039/D2TC03927C.

22. M. Craighero, J. Guo, S. Zokaei, et al., "Impact of Oligoether Side-Chain Length on the Thermoelectric Properties of a Polar Polythiophene," *ACS Applied Electronic Materials* 6, no. 5 (2024): 2909–2916, https://doi.org/10.1021/acsaelm.3c00936.

23. R. Sarabia-Riquelme, R. Andrews, J. E. Anthony, and M. C. Weisenberger, "Highly Conductive Wet-Spun PEDOT:PSS Fibers for Applications in Electronic Textiles," *Journal of Materials Chemistry C* 8, no. 33 (2020): 11618–11630, https://doi.org/10.1039/D0TC02558E.

24. R. Sarabia-Riquelme, L. E. Noble, P. A. Espejo, et al., "Highly Conductive n-Type Polymer Fibers from the Wet-Spinning of n-Doped PBDF and Their Application in Thermoelectric Textiles," *Advanced Functional Materials* 34, no. 9 (2024): 2311379, https://doi.org/10.1002/adfm.202311379.

25. K. Tang, A. Shaw, S. Upreti, et al., "Impact of Sequential Chemical Doping on the Thin Film Mechanical Properties of Conjugated Polymers," *Chemistry of Materials* 37, no. 2 (2025): 756–765, https://doi.org/10.1021/acs.chemmater.4c03120.

26. J. Hynynen, E. Järsvall, R. Kroon, et al., "Enhanced Thermoelectric Power Factor of Tensile Drawn Poly(3-hexylthiophene)," *ACS Macro Letters* 8, no. 1 (2019): 70–76, https://doi.org/10.1021/acsmacrolett.8b00820.

27. A. Lund, N. M. van der Velden, N.-K. Persson, M. M. Hamedi, and C. Müller, "Electrically Conducting Fibres for E-Textiles: an Open Playground for Conjugated Polymers and Carbon Nanomaterials," *Materials*

Science and Engineering: R: Reports 126 (2018): 1–29, https://doi.org/10.1016/j.mser.2018.03.001.

28. N. Kim, S. Lienemann, I. Petsagkourakis, et al., "Elastic Conducting Polymer Composites in Thermoelectric Modules," *Nature Communications* 11, no. 1 (2020): 1424, https://doi.org/10.1038/s41467-020-15135-w.

29. Y. Wang, C. Zhu, R. Pfattner, et al., "A Highly Stretchable, Transparent, and Conductive Polymer," *Science Advances* 3, no. 3 (2017): 1602076, https://doi.org/10.1126/sciadv.1602076.

30. J.-D. Huang, Q. Li, Q. Wang, et al., "Preventing Benzoquinone-Based Catalyst Aggregation Enables the One-Step Synthesis of Highly Conductive Poly(benzodifurandione) without Post-Reaction Purification," *Advanced Materials* 37, no. 17 (2025): 2502426, https://doi.org/10.1002/adma.202502426.

31. J. Mun, J. Kang, Y. Zheng, et al., "F4-TCNQ as an Additive to Impart Stretchable Semiconductors with High Mobility and Stability," *Advanced Electronic Materials* 6, no. 6 (2020): 2000251, https://doi.org/10.1002/aelm.202000251.

32. B. Zhu, J. He, H. Shan, X. Cao, J. Zhou, and H. Huo, "Influence of Different Polymorphs on the Electrical and Mechanical Properties of F4TCNQ-Doped Regioregular P3BT Films," *Macromolecules* 57, no. 9 (2024): 4118–4129, https://doi.org/10.1021/acs.macromol.4c00063.

33. M. L. Le, I. Lapkriengkri, K. R. Albanese, et al., "Engineering Soft, Elastic, and Conductive Polymers for Stretchable Electronics Using Ionic Compatibilization," *Chemistry of Materials* 35, no. 17 (2023): 7301–7310, https://doi.org/10.1021/acs.chemmater.3c01685.

34. V. Untilova, J. Hynynen, A. I. Hofmann, et al., "High Thermoelectric Power Factor of Poly(3-hexylthiophene) through in-Plane Alignment and Doping with a Molybdenum Dithiolene Complex," *Macromolecules* 53, no. 15 (2020): 6314–6321, https://doi.org/10.1021/acs.macromol.0c01223.

35. A. D. Scaccabarozzi, A. Basu, F. Aniés, et al., "Doping Approaches for Organic Semiconductors," *Chemical Reviews* 122, no. 4 (2022): 4420–4492, https://doi.org/10.1021/acs.chemrev.1c00581.

36. T. J. Aubry, J. C. Axtell, V. M. Basile, et al., "Dodecaborane-Based Dopants Designed to Shield Anion Electrostatics Lead to Increased Carrier Mobility in a Doped Conjugated Polymer," *Advanced Materials* 31, no. 11 (2019): 1805647, https://doi.org/10.1002/adma.201805647.

37. Z. Liang, Y. Zhang, M. Souri, et al., "Influence of Dopant Size and Electron Affinity on the Electrical Conductivity and Thermoelectric Properties of a Series of Conjugated Polymers," *Journal of Materials Chemistry A* 6, no. 34 (2018): 16495–16505, https://doi.org/10.1039/C8TA05922E.

38. E. M. Thomas, K. A. Peterson, A. H. Balzer, et al., "Effects of Counter-Ion Size on Delocalization of Carriers and Stability of Doped Semiconducting Polymers," *Advanced Electronic Materials* 6, no. 12 (2020): 2000595, https://doi.org/10.1002/aelm.202000595.

39. I. E. Jacobs, G. D'Avino, V. Lemaur, et al., "Structural and Dynamic Disorder, Not Ionic Trapping, Controls Charge Transport in Highly Doped Conducting Polymers," *Journal of the American Chemical Society* 144, no. 7 (2022): 3005–3019, https://doi.org/10.1021/jacs.1c10651.

40. C. Chen, I. E. Jacobs, K. Kang, et al., "Observation of Weak Counterion Size Dependence of Thermoelectric Transport in Ion Exchange Doped Conducting Polymers across a Wide Range of Conductivities," *Advanced Energy Materials* 13, no. 9 (2023): 2202797, https://doi.org/10.1002/aenm.202202797.

41. K. N. Baustert, J. H. Bombile, M. T. Rahman, et al., "Combination of Counterion Size and Doping Concentration Determines the Electronic and Thermoelectric Properties of Semiconducting Polymers," *Advanced Materials* 36, no. 29 (2024): 2313863, https://doi.org/10.1002/adma.202313863.

42. M. Ishii, Y. Yamashita, S. Watanabe, K. Ariga, and J. Takeya, "Doping of Molecular Semiconductors through Proton-Coupled Electron Transfer," *Nature* 622, no. 7982 (2023): 285–291, https://doi.org/10.1038/s41586-023-06504-8.

43. J. Kimpel, Y. Kim, H. Schomaker, et al., "Open-Flask, Ambient Temperature Direct Arylation Synthesis of Mixed Ionic-Electronic Conductors," *Science Advances* 11, no. 19 (2025): adv8168, https://doi.org/10.1126/sciadv.adv8168.

44. J. Kimpel, Y. Kim, J. Asatryan, J. Martín, R. Kroon, and C. Müller, "High-Mobility Organic Mixed Conductors with a Low Synthetic Complexity Index via Direct Arylation Polymerization," *Chemical Science* 15, no. 20 (2024): 7679–7688, https://doi.org/10.1039/D4SC01430H.

45. J. Moulton and P. Smith, "Electrical and Mechanical Properties of Oriented Poly(3-alkylthiophenes): 2. Effect of Side-chain Length," *Polymer* 33, no. 11 (1992): 2340–2347, https://doi.org/10.1016/0032-3861(92)90525-2.

46. H. Okuzaki and M. Ishihara, "Spinning and Characterization of Conducting Microfibers," *Macromolecular Rapid Communications* 24, no. 3 (2003): 261–264, https://doi.org/10.1002/marc.200390038.

47. H. Okuzaki, Y. Harashina, and H. Yan, "Highly Conductive PEDOT/PSS Microfibers Fabricated by Wet-Spinning and Dip-Treatment in Ethylene Glycol," *European Polymer Journal* 45, no. 1 (2009): 256–261, https://doi.org/10.1016/j.eurpolymj.2008.10.027.

48. Y. Kim, A. Lund, H. Noh, et al., "Robust PEDOT:PSS Wet-Spun Fibers for Thermoelectric Textiles," *Macromolecular Materials and Engineering* 305, no. 3 (2020): 1900749, https://doi.org/10.1002/mame.201900749.

49. R. Kroon, A. I. Hofmann, L. Yu, A. Lund, and C. Müller, "Thermally Activated in Situ Doping Enables Solid-State Processing of Conducting Polymers," *Chemistry of Materials* 31, no. 8 (2019): 2770–2777, https://doi.org/10.1021/acs.chemmater.8b04895.

50. S. Zokaei, "Interplay of the Electrical and Mechanical Properties of Conjugated Polymers," (Chalmers University of Technology, 2022).

51. J. Clark, J.-F. Chang, F. C. Spano, R. H. Friend, and C. Silva, "Determining Exciton Bandwidth and Film Microstructure in Polythiophene Films Using Linear Absorption Spectroscopy," *Applied Physics Letters* 94, (2009): 163306, https://doi.org/10.1063/1.3110904.

52. F. C. Spano and C. Silva, "H- and J-Aggregate Behavior in Polymeric Semiconductors," *Annual Review of Physical Chemistry* 65 (2014): 477–500, https://doi.org/10.1146/annurev-physchem-040513-103639.

53. C. Hellmann, F. Paquin, N. D. Treat, et al., "Controlling the Interaction of Light with Polymer Semiconductors," *Advanced Materials* 25, no. 35 (2013): 4906–4911, https://doi.org/10.1002/adma.201300881.

54. D. Kiefer, R. Kroon, A. I. Hofmann, et al., "Double Doping of Conjugated Polymers with Monomer Molecular Dopants," *Nature Materials* 18, no. 2 (2019): 149–155, https://doi.org/10.1038/s41563-018-0263-6.

55. J. E. Cochran, M. J. N. Junk, A. M. Glaudell, et al., "Molecular Interactions and Ordering in Electrically Doped Polymers: Blends of PBTTT and F4TCNQ," *Macromolecules* 47, no. 19 (2014): 6836–6846, https://doi.org/10.1021/ma501547h.

56. A. L. Dixon, H. Vezin, T.-Q. Nguyen, and G. N. M. Reddy, "Structural Insights into Lewis Acid- and F4TCNQ-doped Conjugated Polymers by Solid-State Magnetic Resonance Spectroscopy," *Materials Horizons* 9, no. 3 (2022): 981–990, https://doi.org/10.1039/D1MH01574E.

57. I. E. Jacobs, F. Wang, N. Hafezi, et al., "Quantitative Dedoping of Conductive Polymers," *Chemistry of Materials* 29, no. 2 (2017): 832–841, https://doi.org/10.1021/acs.chemmater.6b04880.

58. Y. H. Zhao, M. H. Abraham, and A. M. Zissimos, "Fast Calculation of van der Waals Volume as a Sum of Atomic and Bond Contributions and Its Application to Drug Compounds," *The Journal of Organic Chemistry* 68, no. 19 (2003): 7368–7373, https://doi.org/10.1021/jo034808o.

59. M. Gazzano, C. Gualandi, A. Zucchelli, et al., "Structure-Morphology Correlation in Electrospun Fibers of Semicrystalline Polymers by Simultaneous Synchrotron SAXS-WAXD," *Polymer* 63, no. (2015): 154–163, https://doi.org/10.1016/j.polymer.2015.03.002.

60. S. M. Lalwani, C. I. Eneh, and J. L. Lutkenhaus, "Emerging Trends in the Dynamics of Polyelectrolyte Complexes," *Physical Chemistry*

Chemical Physics 22, no. 42 (2020): 24157–24177, https://doi.org/10.1039/D0CP03696J.

61. D. R. Villalva, S. Singh, L. A. Galuska, et al., "Backbone-Driven Host–Dopant Miscibility Modulates Molecular Doping in NDI Conjugated Polymers," *Materials Horizons* 9, no. 1 (2022): 500–508, https://doi.org/10.1039/D1MH01357B.

62. J. Liu, G. Ye, H. G. O. Potgieser, et al., "Amphipathic Side Chain of a Conjugated Polymer Optimizes Dopant Location toward Efficient N-Type Organic Thermoelectrics," *Advanced Materials* 33, no. 4 (2021): 2006694, https://doi.org/10.1002/adma.202006694.

63. D. Scheunemann, E. Järsvall, J. Liu, et al., "Charge Transport in Doped Conjugated Polymers for Organic Thermoelectrics," *Chemical Physics Reviews* 3, no. 2 (2022): 021309, https://doi.org/10.1063/5.0080820.

64. G. Persson, E. Järsvall, M. Röding, et al., "Visualisation of Individual Dopants in a Conjugated Polymer: Sub-Nanometre 3D Spatial Distribution and Correlation with Electrical Properties," *Nanoscale* 14, no. 41 (2022): 15404–15413, https://doi.org/10.1039/D2NR03554E.

65. C. J. Boyle, M. Upadhyaya, P. Wang, et al., "Tuning Charge Transport Dynamics via Clustering of Doping in Organic Semiconductor Thin Films," *Nature Communications* 10, no. 1 (2019): 2827, https://doi.org/10.1038/s41467-019-10567-5.

66. A. Dash, S. Guchait, D. Scheunemann, et al., "Spontaneous Modulation Doping in Semi-Crystalline Conjugated Polymers Leads to High Conductivity at Low Doping Concentration," *Advanced Materials* 36, no. 13 (2024): 2311303, https://doi.org/10.1002/adma.202311303.

67. Y. Zhong, V. Untilova, D. Muller, et al., "Preferential Location of Dopants in the Amorphous Phase of Oriented Regioregular Poly(3-hexylthiophene-2,5-diyl) Films Helps Reach Charge Conductivities of 3000 S cm^{-1}," *Advanced Functional Materials* 32, no. 30 (2022): 2202075, https://doi.org/10.1002/adfm.202202075.

68. S. N. H. M. Yusoff, S. I. A. Halim, A. A. A. Tarmizi, N. F. A. Zainal, and C. C. Han, "Thermal Properties and Morphological Studies of Poly(ethylene oxide) With the Addition of Salt or Nanofiller," *Macromolecular Symposia* 408, no. 1 (2023): 2200065, https://doi.org/10.1002/masy.202200065.

69. S. I. Abdul Halim, C. H. Chan, and H.-W. Kammer, "About Glass Transition in Polymer-Salt Mixtures," *Polymer Testing* 79, (2019): 105994, https://doi.org/10.1016/j.polymertesting.2019.105994.

70. G. Beamson and D. Briggs, *High Relution XPS of Organic Polymers. The Scienta ESCA 300 Database*, (Wiley, 1992).

71. J. Campbell and T. Papp, "Widths of the Atomic K–N7 Levels," *Atomic Data and Nuclear Data Tables* 77, no. 1 (2001): 1–56, https://doi.org/10.1006/adnd.2000.0848.

72. J. F. Moulder and J. Chastain, *Handbook of X-Ray Photoelectron Spectroscopy: A Reference Book of Standard Spectra for Identification and Interpretation of XPS Data*, (Perkin-Elmer Corporation, 1992), 25.

Supporting Information

Additional supporting information can be found online in the Supporting Information section.

Supporting File: adfm73903-sup-0001-SuppMat.docx